Environmental Science & Technology

pubs.acs.org/est

Article

Estimation of Ammonia Emissions over China Using IASI Satellite-Derived Surface Observations

Jianan Chen, Xiaohui Du, Xuejun Liu, Wen Xu,* and Maarten Krol

Cite This: *Environ. Sci. Technol.* 2025, 59, 9991−10000

Read Online

ACCESS | Metrics & More | Article Recommendations | Supporting Information

ABSTRACT: An accurate ammonia (NH_3) emission inventory is crucial for policymakers developing air pollution mitigation strategies. Both satellite observations and bottom-up estimates identify significant NH_3 emission hotspots in China. However, bottom-up NH_3 emission inventories are highly uncertain due to the lack of localized emission factors, while large and uncertain errors in IASI satellite NH_3 columns have hindered their direct application in top-down emission inversion methods. In this study, we perform a top-down optimization of monthly NH_3 emissions over China using IASI-derived surface NH_3 concentrations with well-evaluated error estimates, combined with the CAMx model at a 36 km resolution. Our posterior NH_3 emissions for 2020 (12.3 [10.9−13.6] Tg N yr^{-1}) are significantly higher than prior estimates from the MEIC inventory (7.6 Tg N yr^{-1}), which primarily underestimates emissions during the warm months in hotspot areas (e.g., NCP and MLYR). We employ multiple approaches to comprehensively evaluate our inversion results. Our study highlights that error estimates for low-value observations are a particularly critical factor in the inversion setup, significantly influencing the reliability of emission optimization.

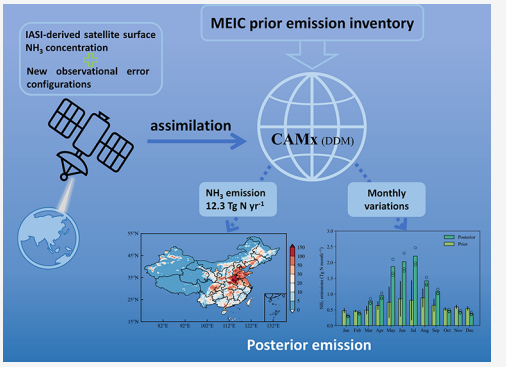

KEYWORDS: *ammonia, emissions over China, IASI satellite observations, emission optimization, agriculture*

1. INTRODUCTION

Nitrogen is an indispensable element for crop growth and global food supply.[1] Since the early 20th century, the Haber-Bosch process has enabled the conversion of inert atmospheric nitrogen (N_2) into ammonia (NH_3) through reaction with hydrogen (H_2). This breakthrough has significantly promoted the production of nitrogen synthetic fertilizers, resulting in a substantial increase in worldwide crop yields.[2] However, the widespread application of nitrogen fertilizers, coupled with reduced usage efficiency,[3] has led to the excessive loss of reactive nitrogen (Nr) to the environment, in the form of NH_3, NH_4^+, NO_3^-, NO_X (= NO & NO_2), and N_2O. This phenomenon has contributed to serious environmental issues, such as $PM_{2.5}$ (fine particulate matter with an aerodynamic diameter < 2.5 μm) air pollution,[4] as well as soil acidification and water eutrophication due to excessive atmospheric nitrogen deposition.[5]

Accurate estimation of NH_3 emissions is crucial for quantifying environmental impacts of Nr loss and assessing mitigation scenarios. Over the last two decades, numerous studies have focused on compiling NH_3 emission inventories at regional and global scales, predominantly employing a bottom-up approach based on emission factors.[6,7] These studies consistently highlight agriculture activities, such as crop fertilization and application of livestock manure, as the predominant sources, contributing approximately 80% to the NH_3 emissions.[8,9] In contrast, other sources, including chemical industry, transportation, biomass burning, and waste disposal, make comparatively minor contributions, although they have shown notable growth in recent years.[10,11] China emerges as a global hotspot for NH_3 emissions, primarily due to its intensive agricultural practices.[12,13] However, significant uncertainties persist in NH_3 emission estimates for China, with variations exceeding a factor of 2 across different assessments, likely due to a lack of detailed emission factors on local scales.[14,15]

Inverse modeling provides a novel option for optimizing emissions by assimilating observational data sets, either from surface monitoring networks or satellite data.[16−18] This optimization (resulting in *a posteriori* or *top-down* emissions) adjusts existing emission inventories (*a priori* or *bottom-up* emissions) to reduce the mismatch between the observed and modeled concentrations driven by the prior emissions.[19]

Ground-based monitoring data provides relatively accurate local surface NH_3 concentrations, but they may not adequately represent the more spatially averaged modeled concentrations. Recent advancements in satellite remote sensing, characterized

Received: October 15, 2024
Revised: May 3, 2025
Accepted: May 5, 2025
Published: May 15, 2025

by high spatial-temporal resolution, present a promising avenue for improving the quantification of the spatiotemporal patterns of NH_3 emissions. This top-down method has been successfully employed in the United States, Europe, and globally using NH_3 column density obtained from instruments such as the Tropospheric Emission Spectrometer (TES), Cross-track Infrared Sounder (CrIS), Atmospheric Infrared Sounder (AIRS), and Infrared Atmospheric Sounding Interferometer (IASI).[17,18,20,21] However, such inversion studies are limited in China. Notably, the top-down NH_3 emission estimates by Zhang et al.,[21] based on the TES satellite, consistently exceeded the values reported by Paulot et al.,[16] who relied on monthly surface measurements of NH_4^+ wet deposition fluxes. A more recent study showed an increasing trend in IASI-derived NH_3 emissions in China from 2008 to 2019.[21] Furthermore, both the annual and monthly NH_3 emissions exhibited varying patterns in previously compiled inventories.[15] Several factors critically affect the utility of satellite infrared (IR) instruments for NH_3 column retrievals. The atmospheric NH_3 abundance and the thermal contrast between the surface and the atmosphere determine how well lower atmospheric NH_3 total column concentrations can be retrieved from the observed radiances. When both the NH_3 concentration and thermal contrast are large, accurate NH_3 column retrievals become feasible.[23] NH_3 columns from IASI exhibit substantial uncertainty, ranging from 5% to over 1000%, with notably poorer performance during winter.[24] This significant uncertainty discourages the direct use of IASI columns in the optimization of NH_3 emission estimates.

However, the NH_3 surface concentrations derived from IASI columns provide a new perspective to optimize NH_3 emissions. While this approach offers more observational data compared to using only sparse in situ measurements, uncertainties in this product remain unexplored. In this study, we aim to constrain monthly NH_3 emissions in China for the year 2020 by integrating well-evaluated surface NH_3 concentrations derived from the IASI satellite total columns[25] into the Comprehensive Air Quality Model (CAMx) with a 36 km grid resolution. In situ measurements from the National Nitrogen Deposition Monitoring Network (NNDMN)[26] are used to evaluate IASI-derived surface NH_3 concentrations and to derive observational error estimates necessary for the inversion. Using a classical big-region inverse modeling technique, we derive monthly fluctuations in NH_3 emissions and their associated errors across six regions in China.

2. METHODS

2.1. IASI Satellite Observations. The IASI instrument is a Fourier transform spectrometer installed on the polar solar-synchronous MetOp-A, -B, and -C meteorological satellites, each launched in different years.[27] MetOp-A has maintained operational stability since the end of 2006 and covers the entire globe twice a day at local times of 9:30 A.M. and P.M. with a nadir footprint of 12 km. The instrument measures infrared radiation in the spectral range of 645−2760 cm^{-1}, emitted by the Earth's surface and the atmosphere. This includes absorption by NH_3 near 950 cm^{-1}, allowing for the retrieval of NH_3 column concentrations.

Over the past years, several improvements have been made in NH_3 column retrievals, which convert the observed spectral NH_3 features into column concentrations. Initially, the brightness temperature differences (BTD) were used for the retrieval.[28] Subsequently, hyperspectral radiation index (HRI) methods were introduced. Whitburn et al.[29] presented a retrieval algorithm based on HRI, followed by NH_3 column conversion using a neural network. Later, a new data set was developed using an artificial neural network for IASI (ANNI) retrieval framework.[24] Currently, two IASI-NH_3 data sets are available: a near-real-time version, which directly utilizes meteorological input data from IASI,[30] and a reanalyzed data set (ANNI-NH_3-v2.1R-I), where the retrieval relies on the European Centre for Medium-Range Weather Forecasts (ECMWF) climate reanalysis data.[24] The latter reanalyzed data set, referred to as ANNI-NH_3-v3R-ERA5, maintains temporal coherence and is particularly suited for trend studies,[31] this is the data set used in the present study.

In this study, we exclusively used daytime IASI columns for the year 2020, as nighttime measurements tend to have larger relative errors due to the generally low thermal contrast.[27] The daily IASI NH_3 column data were spatially mapped onto a 0.1° grid by calculating the arithmetic mean of a set of satellite NH_3 columns within the same grid cell. Subsequently, the monthly average IASI column values were used to derive monthly mean NH_3 surface concentrations. To convert the IASI columns into surface NH_3 concentrations from, two key factors were considered: the modeled NH_3 vertical profile and the surface NH_3 concentration. A vertical profile for each grid cell was derived using Gaussian functions and layered NH_3 concentration data from chemistry transport models (CTMs).[25] The IASI-derived NH_3 surface concentrations, transformed into 24-h mean averages and interpolated to CAMx model grid resolution (Text S1), were used as observations in this study. Since errors in observations play a crucial role in the inversion process, the data product was carefully evaluated by comparing it to surface measurements—not only for spatiotemporal performance, as discussed in Section 3.1, but also by deriving separate relative and absolute errors, as outlined in Section 2.4.

2.2. Ground NH_3 Measurements. The monthly surface NH_3 measurements in the NNDMN are used to assess the satellite-derived surface NH_3 concentrations and evaluate the posterior emissions. This monitoring network, operated by China Agricultural University, serves as a vital long-term platform for national-scale monitoring.[32,33] It consists of 47 monitoring sites distributed across major land-use types (Table S1), including urban, rural (cropland), and background regions (coastal, forest, and grasslands). The locations of the sites are shown in Figure S1. A few sites temporarily shut down due to COVID infection prevention measures. Surface NH_3 concentrations were obtained using both DELTA (Denuder for Long-Term Atmospheric sampling) active sampling systems and α (Adapted Low-cost Passive High Absorption) passive samplers, with a high level of consistency between the two systems (R^2 = 0.9).[33]

2.3. Model Simulations. To relate NH_3 emissions to NH_3 concentrations in the atmosphere, a CTM model is required that describes the major pathways by which NH_3 is transported and transformed. The Comprehensive Air Quality Model with decoupled direct method implemented (CAMx-DDM)[34] is used to perform simulations at a spatial resolution of 36 km × 36 km, with 20 vertical layers extending up to 20 km, covering the entire geographical extent of China within the East Asia domain. The main pathway of gas-phase NH_3 scavenging is through aerosol-forming reactions with H_2SO_4 and HNO_3, with these aerosols subsequently deposited into the terrestrial ecosystem by both dry and wet deposition. The model

https://doi.org/10.1021/acs.est.4c10878
Environ. Sci. Technol. 2025, 59, 9991−10000

employed the SAPRC99 chemical mechanism,[35] and a resistance model for dry deposition.[36] The wet deposition process is represented by an exponential function of the scavenging coefficients.[37] The meteorological fields used to drive simulations in this study are generated using the Weather Research & Forecasting Model (WRF).[38] The performance of the WRF-CAMx model in predicting key pollutants (e.g., sulfate, nitrate, ammonium, and aerosol precursor species) has been evaluated in previous studies.[39,40] The impact of meteorological factors and biases in the CAMx model on optimized emissions will be discussed in Section 3.4.

The anthropogenic NH_3 emission inventory used in this study for China was sourced from the Multiresolution Emission Inventory for Climate and Air Pollution Research[41] (MEIC v1.3) for the base year of 2020. This inventory provides gridded 2-D monthly data for NH_3, as well as other gas and aerosol pollutant emissions, at a spatial resolution of 0.25°. Monthly NH_3 emissions were categorized into sectors, including agriculture, industry, residential, and transportation (Figure S2). For areas outside of China, the Regional Emission inventory in Asia (REAS v2.1)[42] emission inventory for the base year of 2008 was adopted. In this study, NH_3 emissions were considered to originate solely from anthropogenic activities, with natural sources excluded. Gridded 3-D hourly emission inputs required for the CAMx model spatial resolution were produced using the Sparse Matrix Operator Kernel Emissions (SMOKE) modeling system.[43] Further details on the configuration of the CAMx model are provided in Text S2.

For the direct calculation of the sensitivities for a number of parameters simultaneously, the DDM module implemented in the CAMx framework is a computationally efficient method.[44] In this study, the DDM method is employed to simulate the sensitivity of NH_3 concentrations to NH_3 emissions from six distinct regions across China (Figure S1). The resulting hourly sensitivities were transformed into 24-h mean monthly averages, consistent with the observations.

2.4. Inversion Algorithm. Some data assimilation methods, such as four-dimensional variational (4D-Var), are constrained in application by the availability of an adjoint model and computational cost.[45,46] In this study, we select a relatively small number of state vector elements, which makes a traditional basic Bayesian "big region approach" feasible. We divide the entire Chinese domain into six regions and obtain monthly posterior emissions by applying a scaling factor to the prior emissions for each region. Given the limited number of state variables in the current setup (six emission scaling factors for each month), the inversion is computationally efficient and provides the posterior error covariance matrix (see below), which is used to quantify the uncertainty reduction of the prior emission estimates.[47] The monthly posterior emissions ($\hat{\boldsymbol{E}}$) for specific regions are derived by scaling the prior emissions ($\boldsymbol{E}_a$) using the following equation:

$$\hat{\boldsymbol{E}} = \hat{\boldsymbol{x}}\boldsymbol{E}_a \tag{1}$$

The optimal state vector ($\hat{\boldsymbol{x}}$) for prior state vector ($\boldsymbol{x}_a$) is derived as

$$\hat{\boldsymbol{x}} = \boldsymbol{x}_a + (\boldsymbol{K}^T\boldsymbol{S}_O^{-1}\boldsymbol{K} + \boldsymbol{S}_a^{-1})^{-1}\boldsymbol{K}^T\boldsymbol{S}_O^{-1}(\boldsymbol{y} - \boldsymbol{K}\boldsymbol{x}_a) \tag{2}$$

In this context, the observations $\boldsymbol{y}$ represent the monthly IASI-derived surface NH_3 concentrations. The Jacobian matrix $\boldsymbol{K}$, calculated using the DDM method, provides the sensitivity of the simulated observations to the state variable.[47] The matrices $\boldsymbol{S}_O$ and $\boldsymbol{S}_a$ represent the error covariance for observations and for the monthly prior emissions respectively. Both matrices are assumed to be diagonal because we consider each element within them to be independent. Considering the errors on the prior emissions, larger uncertainties were adopted during the summer months when fertilizer and manure is applied. In an iterative procedure, we selected the monthly relative uncertainty on the prior emissions $\boldsymbol{x}_a$ such that $\chi^2 = \frac{(\hat{\boldsymbol{x}} - \boldsymbol{x}_a)^2}{6\boldsymbol{S}_a}$ equals 1, where $\boldsymbol{x}_a$ is the prior emission scaling factor ($\boldsymbol{x}_a = 1$) and $\hat{\boldsymbol{x}}$ is the posterior emission scaling factor. Statistically, this means that the posterior emissions remain within the prescribed error range of the prior emissions, while optimally utilizing the information from the observations.[48] Detailed information about χ^2 and the selected relative uncertainty on the prior emissions is provided in Text S3, S4 and Figure S3.

The errors associated with observations are concentration-dependent. In principle, a relative error is used. However, when only a relative error is configured, low-value observations, which dominate the possibility density function (PDF) pattern of observations (Figure S4), receive a small error that begins to dominate the cost function (Text S3). We found that, as a result, the optimal emissions would be underestimated. For this reason, we configured a concentration-dependent error (in μg N m^{-3}) that consists of a 30% relative error and a 1 μg N m^{-3} absolute error. This was done by analyzing the observational PDF, the cost function, and comparing it to the NNDMN in situ measurements. The derivation of $\boldsymbol{S}_O$ is detailed in Text S5 and Figure S5. To evaluate the impact of the error configurations on the optimized emissions, we performed different inversions with alternative error settings, as discussed in Section 3.4.

The inversion method provides the posterior error covariance matrix $\boldsymbol{S}_p$:

$$\boldsymbol{S}_p = (\boldsymbol{K}^T\boldsymbol{S}_O^{-1}\boldsymbol{K} + \boldsymbol{S}_a^{-1})^{-1} \tag{3}$$

This estimate quantifies the reductions in errors of the prior emissions ($\boldsymbol{S}_a$) and it is used to calculate the posterior standard deviation (σ) per month, per region and for the total annual emissions. Detailed information is provided in Text S6.

3. RESULTS

3.1. IASI-Derived Surface NH_3 Concentration. The annual mean NH_3 surface concentration over China in 2020, derived from IASI satellite observations, was 3.8 (range: 0.1 to 34.8 μg N m^{-3}) (Figure S6). The highest regionally averaged NH_3 concentrations were observed in the North China Plain (NCP), with a value of 16.5 μg N m^{-3} (Figure S7). Additionally, high NH_3 concentrations were identified in the Middle and Lower Yangtze River (MLYR) region (regional mean of 7.4 μg N m^{-3}), and in the northwestern area of Xinjiang Province, which had a maximum value of 21.7 μg N m^{-3}. The surface NH_3 concentrations in summer are significantly higher than those in winter (Figure S8). The highest average NH_3 concentration over China occurred in July (7.0 μg N m^{-3}) while the lowest was in January (2.5 μg N m^{-3}). This significant seasonal variation is consistent with the variations observed in total satellite columns from IASI (Figure S9), AIRS[49] and GIIRS.[22]

Before conducting the emission inversion, the IASI-derived surface NH_3 concentrations were assessed by comparing them

https://doi.org/10.1021/acs.est.4c10878
Environ. Sci. Technol. 2025, 59, 9991−10000

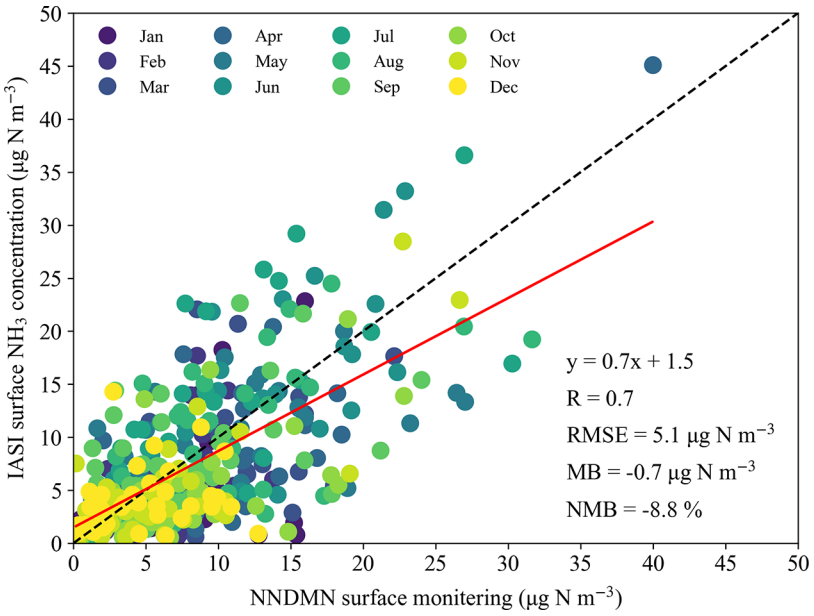

Figure 1. Comparison of the IASI-derived monthly NH_3 surface concentrations and the NNDMN monthly average measurements for 2020.

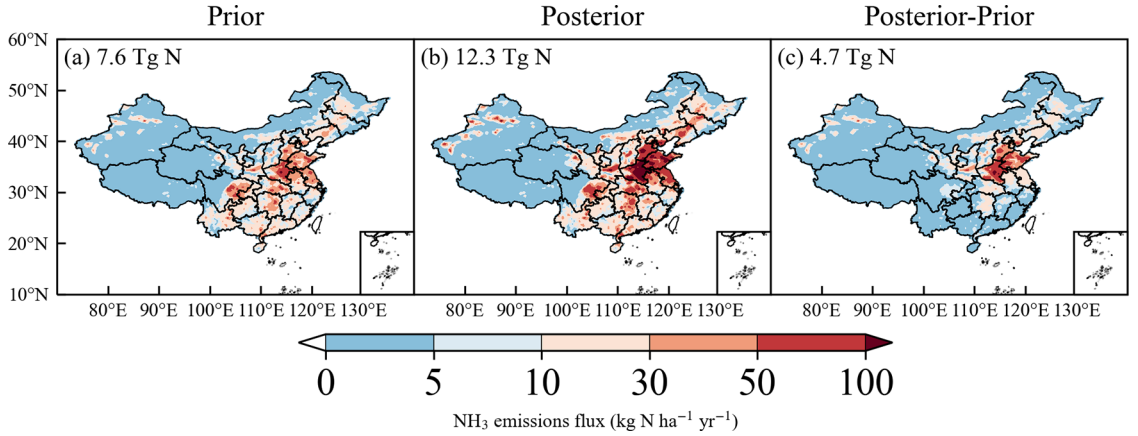

Figure 2. Spatial distributions of (a) the prior and (b) the posterior annual NH_3 emissions over China in 2020, and of (c) the posterior minus prior emissions estimates.

with in situ measurements. The measured NH_3 concentrations were generally well captured by IASI estimates, showing a correlation coefficient of 0.7 (Figure 1) and a normalized mean bias (NMB) of only −8.8%. However, the IASI surface estimates notably underestimated NH_3 concentrations in the Northeast (NE), South China (SC) and Southwest (SW) regions, with mean bias errors (MB) of −2.0, −1.5, and −1.3 μg N m^{-3}, respectively (Figure S10). In contrast, there was strong agreement between IASI-derived surface NH_3 concentrations and NNDMN measurements in the MLYR and NCP regions. We also assessed the IASI-derived NH_3 estimates for the different seasons (Figure S11). The surface NH_3 concentrations were poorly represented by the IASI-derived data in January, exhibiting an MB of −2.0 μg N m^{-3} and R = 0.4. This suggests potential underestimations in IASI-derived surface NH_3 due to the limited NH_3 abundance, lower temperatures and lower thermal contrast during the winter season. Moreover, errors in the model's vertical profile, and inaccuracies in the representation of the derived surface data may also contribute to the discrepancies.[25]

3.2. Posterior NH_3 Emissions. Figure 2 shows the spatial distributions of the prior and posterior annual NH_3 emissions and the differences between them. The posterior annual emission is 12.3 Tg N yr^{-1}, reflecting a substantial 62% increase compared to the prior estimate of 7.6 Tg N yr^{-1}. The posterior emissions generally show an increase across China. The most significant emission increases are observed in the NCP and Northwest (NW) regions, where the posterior NH_3 emissions are more than twice those of the prior estimates. In contrast, the SC and SW regions show smaller increases, with increments of only 17% (0.14 Tg N yr^{-1}) and 14% (0.21 Tg N yr^{-1}), respectively (Figure S12). The SC region is characterized by a smaller agricultural production, but highly developed transportation infrastructure, a large population and intensive industrial activity.[11]

High NH_3 emissions are consistently observed in the NCP and MLYR regions, and the Sichuan basin in both the prior and posterior estimates, with the largest differences between the two estimates also occurring in these regions. The NCP region, which includes the provinces of Beijing, Tianjin, Hebei, Henan, and Shandong, has the largest NH_3 emissions in China,

https://doi.org/10.1021/acs.est.4c10878
Environ. Sci. Technol. 2025, 59, 9991−10000

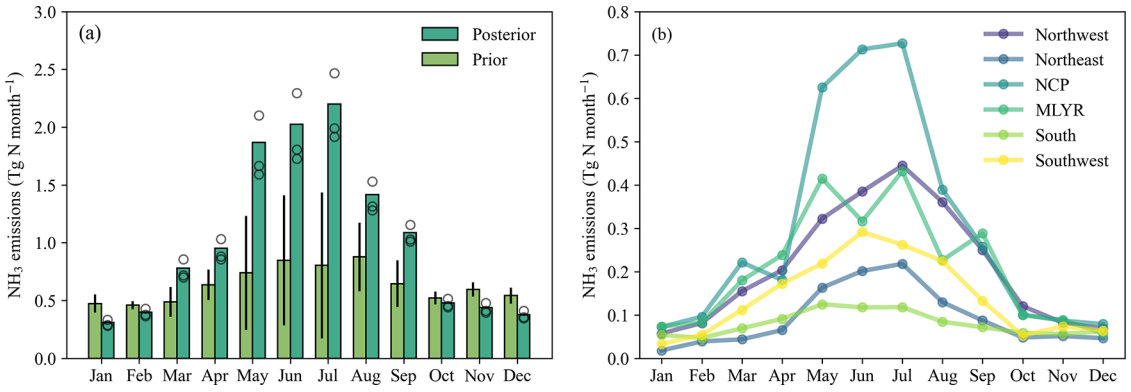

Figure 3. Monthly variations in posterior NH_3 emissions for 2020 over (a) the whole of China and (b) six individual regions. The circles in panel (a) represent uncertainties in posterior emissions, derived from performing inversions with alternative observational error configurations, as will be discussed in Section 3.4.

with an optimized maximum emission intensity exceeding 100 kg N ha^{-1} yr^{-1}. In the posterior estimates, considerable emissions are also observed in the Sichuan basin, as well as in the NE and MLYR regions, surpassing the levels of the prior estimates and reaching values close to those of the NCP region. Although our posterior emissions represent total amounts, the pattern of high-emission regions aligns with areas characterized by significant agricultural activities, as inferred from the geographic distribution of cropland in 2020 (Figure S13) and livestock production.[50,51] This suggests that agricultural emissions may have been underestimated in the MEIC. Additionally, local underestimations may result from sources with relatively minor regional contributions but high local emission densities, such as industry and residential, as indicated by the spatial distribution in the prior emissions (Figure S2).

3.3. Monthly Variations. The posterior NH_3 emissions exhibit distinct seasonal variations, as shown in Figure 3a. The total emissions during the summer months (May–July) were 6.1 Tg N, approximately five times higher than those in the winter months (1.1 Tg N, November–February). The optimized NH_3 emissions display an ascending trend starting in January, peaking in July, and gradually declining thereafter. This seasonal pattern aligns with the findings from recent inversion studies, which contrast with existing bottom-up studies that report peak values in June and August (Figures S14 and S15).

Due to its pronounced seasonality and status as the largest contributor to NH_3 emissions, agriculture has emerged as the most important factor influencing monthly variations in NH_3 emissions compared to other sectors, such as residential, transportation, and industry. These latter sectors make only minor contributions to the total emissions and show relatively constant year-round emissions (Figure S16). Monthly fluctuations in agricultural emissions are influenced by a combination of farming practices (including timings of cultivation and fertilization) and environmental factors, such as temperature, soil properties, and wind speed. Agricultural sources primarily include livestock waste and cropland. Monthly variations in livestock emissions are mainly attributed to meteorological factors, such as higher temperatures in summer, because there are minimal fluctuations in livestock populations across different months.[8,52] In the case of cropland emissions, monthly variations are primarily driven by specific fertilization practices tailored to different crops, which coincide with environmental factors. In most regions of China, various crops are sowed with base fertilization in April, followed by additional top dressing in the subsequent 1–2 months.[8] A significant proportion (approximately 70%) of nitrogen fertilizer is applied through injection and broadcast methods from April to August.[21] This, coupled with the increasing air temperature,[52] leads to emissions during the warmer months (April–September).

The monthly variations in NH_3 emissions across six regions are shown in Figures 3b and S17. The posterior emissions reveal varied seasonal fluctuations in the six regions, primarily attributed to planting patterns (including seeding and fertilization timing for multiple crop categories) and differing environmental conditions across China, from north to south. A clear peak in July is observed in the NCP region, which is attributed to the prevalent winter wheat-summer maize rotation system, a distinctive farming practice in this region.[53] Moreover, the alkaline soil properties in northern China can further enhance temperature-dependent NH_3 volatilization.[54] The NW region covers a vast area, and a large fraction of this region has low grain production due to its arid climate. However, the northwestern part of Xinjiang province is notable for its intensive livestock farming. The MLYR and SW regions are characterized by widespread paddy rice and vegetable cultivation, with sowing beginning in March-April.[55,56] The higher NH_3 volatilization rates in paddy fields (14.8%) compared to upland soils (11.8%) may be a key driver contributing to the larger monthly emissions observed in the MLYR regions compared to dry areas.[55,57] In contrast, the SC region does not exhibit a prominent summer peak in NH_3 emissions because of urbanization and limited agricultural activity. Both nonagricultural and agricultural sources are important contributors to NH_3 in the urban atmosphere.[8,58]

3.4. Validation of the Optimized Emission Estimates. We use five approaches to comprehensively evaluate the optimal emission estimates obtained from the 12 monthly inversions. First, we assess the impact of error configuration on the posterior emissions and cost function. The posterior emissions do not change significantly with different choices of error characteristics for prior emissions (Figures S18 and S19), which can be attributed to the small weight of the background component in the total cost function (Text S3). However, the optimal estimates are more sensitive to the choice of observational errors (Figure S20) when we perform the inversion program with different combinations of relative and

https://doi.org/10.1021/acs.est.4c10878
Environ. Sci. Technol. 2025, 59, 9991–10000

absolute errors. Low concentrations (< 1 μg N m^{-3}) dominate the observational data set across China, as shown by the probability density function (PDF) of observations (Figure S4). If a small error is assigned to these low-concentration observations, they would have a disproportionately large weight in the cost function (Text S3), leading to an underestimation of emissions. This highlights the importance of absolute error, as errors in low concentrations are primarily influenced by this component. A proper error setting for small observations can be determined by analyzing the observational component of the posterior χ^2 (Text S4). Ideally, concentrations modeled with the posterior emissions ($\boldsymbol{K}\hat{\boldsymbol{x}}$) should exhibit zero bias and normally distributed deviations from the observations ($\boldsymbol{y}$), with a mean σ value close to the prescribed observational error. Following this principle, an absolute error of 0.5−1.0 μg N m^{-3}, combined with a 30% relative error, proves to be a reasonable choice in our study, as shown in Figures S21 and S22. In general, the outliers in Figure S21 are negative, indicating that the model overestimates several high observations. Simply put, an excessively large error for small observations places more weight on high observations, leading to higher optimal emission estimates. Conversely, smaller errors for low observations result in lower optimal emission estimates.

Second, the error reductions are evaluated (Text S6). The posterior standard deviations of the monthly, regional and annual total emissions show a significant reduction compared to the prescribed errors in the prior emissions (Tables S3 and S4). The prior uncertainty of 0.6 Tg N in July declines to 0.1 Tg N in the posterior emissions. When aggregating the error for the annual total NH_3 emissions in China, the posterior error appears unrealistically low at 0.1 Tg N yr^{-1}. This suggests that the large number of observations, combined with a relatively small number of unknown scaling factors that are optimized, results in a well-constrained system. We believe that a realistic error in the optimized emissions is likely much larger because: (1) our results are sensitive to the error settings: when we vary these errors within a realistic range, the yearly total optimized emissions fall within the range of 10.9−13.6 Tg N yr^{-1} (Figure S20); (2) there may be errors in model parameters that link emissions to atmospheric observations, including uncertainties in the chemistry and deposition of NH_x; (3) the observations used in this study have large uncertainties and generally underestimate the surface concentrations from the NNDMN network in winter (Section 3.1 and Figure S11). After correcting this for the winter bias, we find that the optimized winter emissions increase by approximately 0.5 Tg (Figure S23).

The third evaluation concerns the inversion algorithm outlined in Text S4. The posterior cost function decreases compared to the prior one (Figure S19). By validating the predicted posterior NH_3 concentrations match to IASI-derived surface observations, the gap is noticeably reduced (Figure S24). It is important to note that the optimized emissions were derived under the assumption of a linear relationship between emissions and atmospheric surface concentration, by $\mathbf{Kx}$ in the inversion. However, this relationship is likely not linear due to nonlinear chemistry processes. To assess the effect of these nonlinearities, we compared the posterior concentrations ($\boldsymbol{K}\hat{\boldsymbol{x}}$, referred to as the linear model) to the CAMx rerun simulations ($\boldsymbol{K}(\hat{\boldsymbol{x}})$, referred to as the nonlinear model). Figure 4 illustrates a strong correlation between the linear model and the nonlinear CAMx model. Overall, the nonlinearities in the emission−concentration relationship result in slightly lower NH_3 concentrations compared to those predicted by the linear model. One could argue that accounting for the nonlinear emission-concentration relationship would require slightly larger positive emission increments than those obtained from the linear inversion.

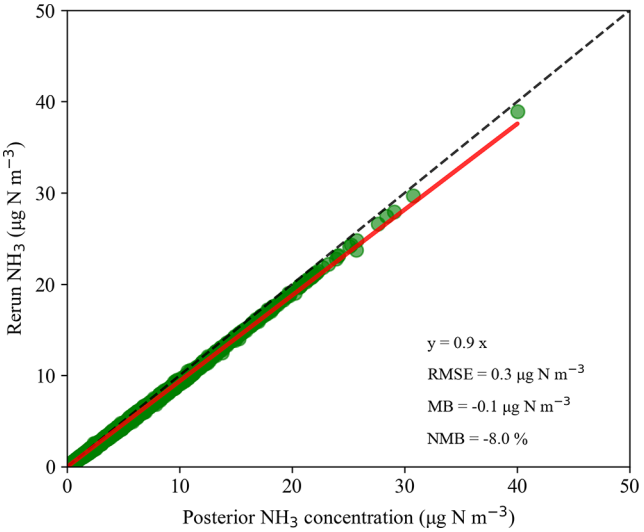

Figure 4. Comparison of gridded NH_3 concentrations over China simulated by model rerun $\boldsymbol{K}(\hat{\boldsymbol{x}})$ and the posterior estimates $\boldsymbol{K}\hat{\boldsymbol{x}}$.

Fourth, the spatial distribution and seasonal variations in the posterior emissions are evaluated by comparing simulations to in situ NH_x ($\equiv NH_3 + NH_4^+$) measurements, which have been suggested to be a more robust indicator of model performance than NH_3 concentrations alone.[59] The spatial distribution is assessed by comparing annual average NH_x per site, as shown in panels (a) and (b) of Figure S25. The annual average NH_x in the prior run is generally underestimated and shows only a small correlation with measurements (MB = −8.2 μg N m^{-3}, slope = 0.2). The fit is significantly improved in the rerun with the posterior emission. Next, the temporal distribution is evaluated using the same set of measurements but on a monthly average basis, as shown in panels (c) and (d) of Figure S25. The modeled monthly NH_x concentrations in the prior simulations show a clear underestimate and a large discrepancy compared to the measurements (R = 0.4, slope = 0.2). The rerun with the posterior emissions leads to a substantial improvement, with a higher correlation (R = 0.6, slope = 0.5) and smaller biases. While emissions play a crucial role, measurement uncertainties also contribute to discrepancies between measured and predicted NH_x. Systematic biases in sampling and analytical procedures may affect observed concentrations. Additionally, spatial resolution is a key factor:[60] surface measurements reflect local conditions, whereas model simulations represent grid-cell averages, making direct comparisons inherently challenging. This issue is particularly significant for NH_3, which has a short atmospheric lifetime and undergoes rapid scavenging processes. Furthermore, uncertainties in the modeling of chemical and physical processes, such as gas-aerosol partitioning and deposition, can substantially influence NH_x predictions. We select NH_x as an evaluation metric to mitigate uncertainties in gas-aerosol partitioning; however, limitations in the model's deposition parametrization may still bias the comparisons. For instance,

https://doi.org/10.1021/acs.est.4c10878
Environ. Sci. Technol. 2025, 59, 9991−10000

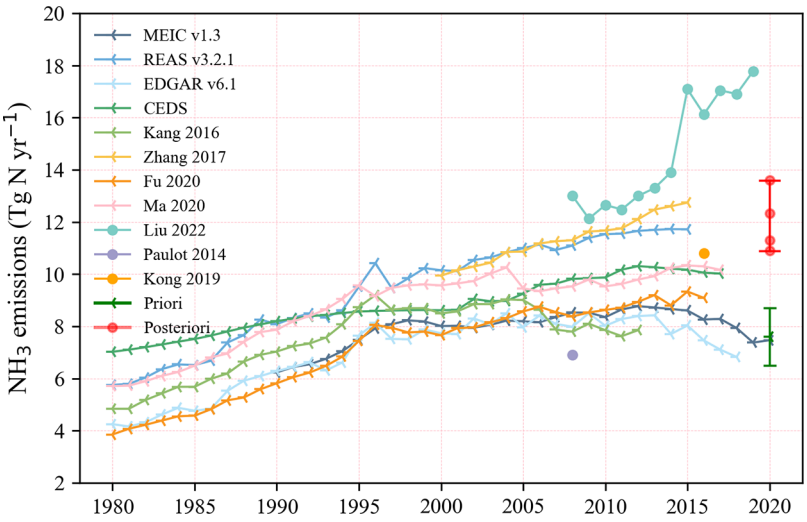

Figure 5. Comparison of NH_3 emissions in China from published results and data sets (Tables S5 and S6). Note that the posterior error is taken as the range from inversions (red circles) with different error settings on the observations. Studies represented by circles indicate NH_3 emissions estimated using the inversion model method.

overestimating deposition velocity would artificially reduce simulated NH_x concentrations.

Finally, we conducted a comparative assessment with several existing studies to evaluate our posterior NH_3 estimates in terms of magnitude, spatial distribution, and seasonal variations. Our optimized NH_3 emissions, obtained through the assimilation of IASI-derived surface NH_3 concentrations data in China for the year 2020, increased from 7.6 ± 1.1 Tg N yr^{-1} to 12.3 (10.9−13.6) Tg N yr^{-1}, representing a 78% increase compared to the 6.9 Tg N yr^{-1} estimate from Paulot et al.[16] and a significant increase relative to most bottom-up estimates (Figure 5). However, the optimized emissions are 45% lower than those of Liu et al.[22] (17.8 Tg N yr^{-1} in 2019), who used a mass balance method based on the same observations as those used in our study[22]. Our optimized emissions are roughly consistent with the estimates of Kong et al.[61] (10.8 Tg N yr^{-1} in 2016), who used an Ensemble Kalman Filter (EnKF) method combined with monthly NH_3 concentrations from a surface measurement network. These disparities are mainly attributed to the approach used to estimate NH_3 emissions, variations in the observation data sets used for inversion and differences in the base years. The spatial distributions of recently developed bottom-up NH_3 emission data sets are shown in Figure S26, based on the up-to-date available year. Our estimates are generally aligned with the REAS estimates in hotspot regions but show notable discrepancies with EDGAR and CEDS. Most of the bottom-up inventories consistently report much lower NH_3 emissions than our optimized estimates in NCP and MLYR regions. A comparison of the monthly variations between our posterior NH_3 emissions and previous estimates is presented in Figures S14 and S15. The monthly NH_3 emission patterns vary considerably among inventories. Although our optimized emissions align with bottom-up estimates during the winter months, they are significantly higher in summer, with a noticeable peak in July. This divergence reflects the substantial uncertainty in summer NH_3 emissions, which is associated with the complexity of agricultural practices at fine temporal resolutions and the substantial influence of environmental conditions on emission factors.

We performed inversions with different error settings and found that the inversion solution is highly sensitive to these settings, particularly for observations with low concentrations. An ill-defined error for low-value observations can easily lead to erroneous emission estimates. In our final approach to selecting observational errors, we determined that a combination of a 30% relative error and an absolute error of 0.5−1 μg N m^{-3} is consistent with surface monitoring network data and results in realistic inversion outcomes. Additionally, we focused on the linearization problem of the inverse, the calculation of error reduction in the posterior, comparisons with surface measurements, and previous studies.

While the "big-region" approach provides useful emission estimates, biases in the model inputs and equations play a crucial role in the inversion process by strongly influencing NH_x prediction through transport, and dispersion, chemical interactions. First, WRF-simulated meteorological fields were evaluated using hourly surface measurements (Figures S27−30). Overall, WRF successfully replicates observed meteorological conditions. However, WRF generally underestimates wind speed, potentially leading to higher predicted NH_3 concentrations and subsequently underestimated emissions. Conversely, the underestimated temperature over region "South". which enhances NH_3 partitioning into aerosols in the model, would result in overestimated optimized emissions. Additionally, higher modeled precipitation would lead to overestimated emissions due to more deposition and smaller NH_3 atmospheric concentrations.

Second, biases in acid gas emissions can also affect NH_3 predictions. For instance, gas-phase NH_3 is often underpredicted when sulfate is overestimated,[62] reducing NH_3 sensitivity to emissions and leading to overpredicted optimized emissions. Third, uncertainties in model numeric, gas-aerosol partitioning, and deposition velocity further influence optimized emissions. Balasubramanian (2020) summarized CAMx model evaluations from previous studies, which showed consistent underpredictions of NH_3 concentrations. One possible reason is the overestimated NH_3 deposition, as CAMx currently does not model bidirectional NH_3 exchange, which takes canopy compensation points into account to predict ambient NH_3 concentrations. The introduction of

https://doi.org/10.1021/acs.est.4c10878
Environ. Sci. Technol. 2025, 59, 9991−10000

bidirectional exchange in the LOTOS-EUROS model increased NH_3 concentration predictions by 30−40% due to the longer NH_3 lifetime.[63] In contrast, higher partitioning to the aerosol phase reduces NH_3 atmospheric concentrations, potentially leading to an overestimation of inverted emissions.

To mitigate these biases and to improve inversion estimates, future work could: (1) project the native-resolution state vector onto several representative states using alternative techniques, such as the Gaussian Mixture Model (GMM) or reduced-dimension/rank inversions.[19,64] These methods could improve the spatial distribution of emissions. (2) directly integrate multi-satellite NH_3 observations (e.g., from CrIS and GIIRS) into CTM.[17,65] This could offer a promising avenue for improving the spatial-temporal resolution and reducing biases. (3) conduct multi-year simulations to analyze interannual variability driven by meteorology and its impact on optimized NH_3 emissions, providing a more comprehensive assessment.

■ ASSOCIATED CONTENT

Supporting Information

The Supporting Information is available free of charge at https://pubs.acs.org/doi/10.1021/acs.est.4c10878.

Description of observational data, model configuration, cost function, inversion evaluation and error estimates. Evaluation of observations. Quantify observational errors. Validation of posterior emissions. Sites of NNDMN. Error estimation by month and region. Comparison with previous studies (PDF)

■ AUTHOR INFORMATION

Corresponding Author

Wen Xu − *State Key Laboratory of Nutrient Use and Management, College of Resources and Environmental Sciences, National Academy of Agriculture Green Development, National Observation and Research Station of Agriculture Green Development (Quzhou, Hebei), China Agricultural University, Beijing 100193, China;* orcid.org/0000-0001-5264-7445; Email: wenxu@cau.edu.cn

Authors

Jianan Chen − *State Key Laboratory of Nutrient Use and Management, College of Resources and Environmental Sciences, National Academy of Agriculture Green Development, National Observation and Research Station of Agriculture Green Development (Quzhou, Hebei), China Agricultural University, Beijing 100193, China; Meteorology and Air Quality Group, Wageningen University & Research, Wageningen 6708 PB, Netherlands;* orcid.org/0009-0006-8033-6373

Xiaohui Du − *State Key Laboratory of Environmental Criteria and Risk Assessment, Chinese Research Academy of Environmental Sciences, Beijing 100012, China*

Xuejun Liu − *State Key Laboratory of Nutrient Use and Management, College of Resources and Environmental Sciences, National Academy of Agriculture Green Development, National Observation and Research Station of Agriculture Green Development (Quzhou, Hebei), China Agricultural University, Beijing 100193, China;* orcid.org/0000-0002-8367-5833

Maarten Krol − *Meteorology and Air Quality Group, Wageningen University & Research, Wageningen 6708 PB, Netherlands; Institute for Marine and Atmospheric Research Utrecht, Utrecht University, Utrecht 3526KV, Netherlands*

Complete contact information is available at: https://pubs.acs.org/10.1021/acs.est.4c10878

Author Contributions

W.X. and M.K. designed the study. J.C. performed the data analysis and prepared the figures and tables. J.C., M.K., and W.X. wrote the manuscript. X.D. helped to perform the CAMx model. All authors were involved in the discussion and the revision of the manuscript.

Notes

The authors declare no competing financial interest.

■ ACKNOWLEDGMENTS

This study was supported by National Natural Science Foundation of China (42175137), the Major Science and Technology Project of Yunnan Province (202202AE090034), the National Key Research and Development Program of China (2021YFD1700902, 2023YFD1702103), Cheung Kong Scholars Program, and China Scholarship Council (No.201913043). We acknowledge the free use of IASI satellite column data (https://iasi.aeris-data.fr/nh3/). We acknowledge Lei Liu and Pu Liu (College of Earth and Environmental Sciences, Lanzhou University) for providing IASI-derived surface NH_3 concentrations data, and Mathew R. Heal at the University of Edinburgh for his valuable comments on this manuscript.

■ REFERENCES

(1) Gruber, N.; Galloway, J. N. An Earth-system perspective of the global nitrogen cycle. *Nature* **2008**, *451*, 293−296.

(2) Zhang, X.; Zou, T.; Lassaletta, L.; Mueller, N. D.; Tubiello, F. N.; Lisk, M. D.; Lu, C.; Conant, R. T.; Dorich, C. D.; Gerber, J.; Tian, H.; Bruulsema, T.; Maaz, T. M.; Nishina, K.; Bodirsky, B. L.; Popp, A.; Bouwman, L.; Beusen, A.; Chang, J.; Havlík, P.; Leclère, D.; Canadell, J. G.; Jackson, R. B.; Heffer, P.; Wanner, N.; Zhang, W.; Davidson, E. A. Quantification of global and national nitrogen budgets for crop production. *Nat. Food* **2021**, *2*, 529−540.

(3) Lassaletta, L.; Billen, G.; Grizzetti, B.; Anglade, J.; Garnier, J. 50 year trends in nitrogen use efficiency of world cropping systems: the relationship between yield and nitrogen input to cropland. *Environ. Res. Lett.* **2014**, *9*, No. 105011.

(4) Xu, W.; Zhao, Y.; Wen, Z.; Chang, Y.; Pan, Y.; Sun, Y.; Ma, X.; Sha, Z.; Li, Z.; Kang, J.; Liu, L.; Tang, A.; Wang, K.; Zhang, Y.; Guo, Y.; Zhang, L.; Sheng, L.; Zhang, X.; Gu, B.; Song, Y.; Van Damme, M.; Clarisse, L.; Coheur, P.-F.; Collett, J. L., Jr.; Goulding, K.; Zhang, F.; He, K.; Liu, X. Increasing importance of ammonia emission abatement in $PM_{2.5}$ pollution control. *Sci. Bull.* **2022**, *67*, 1745−1749.

(5) Feng, S. J.; Wang, M. R.; Heal, M. R.; Liu, X. J.; Liu, X. Y.; Zhao, Y. H.; Strokal, M.; Kroeze, C.; Zhang, F. S.; Xu, W. The impact of emissions controls on atmospheric nitrogen inputs to Chinese river basins highlights the urgency of ammonia abatement. *Sci. Adv.* **2024**, *10*, No. eadp2558.

(6) Liu, L.; Xu, W.; Lu, X.; Zhong, B.; Guo, Y.; Lu, X.; Zhao, Y.; He, W.; Wang, S.; Zhang, X.; Liu, X.; Vitousek, P. Exploring global changes in agricultural ammonia emissions and their contribution to nitrogen deposition since 1980. *Proc. Natl. Acad. Sci. U.S.A.* **2022**, *119*, No. e2121998119.

(7) McDuffie, E. E.; Smith, S. J.; O'Rourke, P.; Tibrewal, K.; Venkataraman, C.; Marais, E. A.; Zheng, B.; Crippa, M.; Brauer, M.; Martin, R. V. A global anthropogenic emission inventory of atmospheric pollutants from sector- and fuel-specific sources (1970−2017): an application of the Community Emissions Data System (CEDS). *Earth Syst. Sci. Data* **2020**, *12*, 3413−3442.

(8) Li, B.; Chen, L.; Shen, W.; Jin, J.; Wang, T.; Wang, P.; Yang, Y.; Liao, H. Improved gridded ammonia emission inventory in China. *Atmos. Chem. Phys.* **2021**, *21*, 15883−15900.
(9) Huang, X.; Song, Y.; Li, M.; Li, J.; Huo, Q.; Cai, X.; Zhu, T.; Hu, M.; Zhang, H. A high-resolution ammonia emission inventory in China. *Global Biogeochem. Cycles* **2012**, *26*, No. GB1030.
(10) Xu, J.; Lu, M.; Guo, Y.; Zhang, L.; Chen, Y.; Liu, Z.; Zhou, M.; Lin, W.; Pu, W.; Ma, Z.; Song, Y.; Pan, Y.; Liu, L.; Ji, D. Summertime Urban Ammonia Emissions May Be Substantially Underestimated in Beijing, China. *Environ. Sci. Technol.* **2023**, *57*, 13124−13135.
(11) Ma, S. High-resolution assessment of ammonia emissions in China: Inventories, driving forces and mitigation. *Atmos. Environ.* **2020**, *229*, No. 117458.
(12) Yang, Y.; Liu, L.; Bai, Z.; Xu, W.; Zhang, F.; Zhang, X.; Liu, X.; Xie, Y. Comprehensive quantification of global cropland ammonia emissions and potential abatement. *Sci. Total Environ.* **2022**, *812*, No. 151450.
(13) Zhan, X.; Adalibieke, W.; Cui, X.; Winiwarter, W.; Reis, S.; Zhang, L.; Bai, Z.; Wang, Q.; Huang, W.; Zhou, F. Improved estimates of ammonia emissions from global croplands. *Environ. Sci. Technol.* **2021**, *55*, 1329−1338.
(14) Chen, J.; Cheng, M.; Krol, M.; de Vries, W.; Zhu, Q.; Liu, X.; Zhang, F.; Xu, W. Trends in anthropogenic ammonia emissions in China since 1980: A review of approaches and estimations. *Front. Environ. Sci.* **2023**, *11*, No. 1133753, DOI: 10.3389/fenvs.2023.1133753.
(15) Ma, R.; Zou, J.; Han, Z.; Yu, K.; Wu, S.; Li, Z.; Liu, S.; Niu, S.; Horwath, W. R.; Zhu-Barker, X. Global soil-derived ammonia emissions from agricultural nitrogen fertilizer application: A refinement based on regional and crop-specific emission factors. *Global Change Biol.* **2021**, *27*, 855−867.
(16) Paulot, F.; Jacob, D. J.; Pinder, R. W.; Bash, J. O.; Travis, K.; Henze, D. K. Ammonia emissions in the United States, European Union, and China derived by high-resolution inversion of ammonium wet deposition data: Interpretation with a new agricultural emissions inventory (MASAGE_NH3). *J. Geophys. Res.:Atmos.* **2014**, *119*, 4343−4364.
(17) van der Graaf, S.; Dammers, E.; Segers, A.; Kranenburg, R.; Schaap, M.; Shephard, M. W.; Erisman, J. W. Data assimilation of CrIS NH_3 satellite observations for improving spatiotemporal NH_3 distributions in LOTOS-EUROS. *Atmos. Chem. Phys.* **2022**, *22*, 951−972.
(18) Marais, E. A.; Pandey, A. K.; Van Damme, M.; Clarisse, L.; Coheur, P. F.; Shephard, M. W.; Cady-Pereira, K. E.; Misselbrook, T.; Zhu, L.; Luo, G.; Yu, F. UK ammonia emissions estimated with satellite observations and GEOS-Chem. *J. Geophys. Res.:Atmos.* **2021**, *126*, No. e2021JD035237, DOI: 10.1029/2021JD035237.
(19) Turner, A. J.; Jacob, D. J. Balancing aggregation and smoothing errors in inverse models. *Atmos. Chem. Phys.* **2015**, *15*, 7039−7048.
(20) Jin, J.; Fang, L.; Li, B.; Liao, H.; Wang, Y.; Han, W.; Li, K.; Pang, M.; Wu, X.; Xiang Lin, H. 4DEnVar-based inversion system for ammonia emission estimation in China through assimilating IASI ammonia retrievals. *Environ. Res. Lett.* **2023**, *18*, No. 034005.
(21) Zhang, L.; Chen, Y.; Zhao, Y.; Henze, D. K.; Zhu, L.; Song, Y.; Paulot, F.; Liu, X.; Pan, Y.; Lin, Y.; Huang, B. Agricultural ammonia emissions in China: reconciling bottom-up and top-down estimates. *Atmos. Chem. Phys.* **2018**, *18*, 339−355.
(22) Liu, P.; Ding, J.; Liu, L.; Xu, W.; Liu, X. Estimation of surface ammonia concentrations and emissions in China from the polar-orbiting Infrared Atmospheric Sounding Interferometer and the FY-4A Geostationary Interferometric Infrared Sounder. *Atmos. Chem. Phys.* **2022**, *22*, 9099−9110.
(23) Warner, J. X.; Wei, Z.; Strow, L. L.; Dickerson, R. R.; Nowak, J. B. The global tropospheric ammonia distribution as seen in the 13-year AIRS measurement record. *Atmos. Chem. Phys.* **2016**, *16*, 5467−5479.
(24) Van Damme, M.; Whitburn, S.; Clarisse, L.; Clerbaux, C.; Hurtmans, D.; Coheur, P.-F. Version 2 of the IASI NH_3 neural network retrieval algorithm: near-real-time and reanalysed datasets. *Atmos. Meas. Tech.* **2017**, *10*, 4905−4914.
(25) Liu, L.; Zhang, X.; Wong, A. Y. H.; Xu, W.; Liu, X.; Li, Y.; Mi, H.; Lu, X.; Zhao, L.; Wang, Z.; Wu, X.; Wei, J. Estimating global surface ammonia concentrations inferred from satellite retrievals. *Atmos. Chem. Phys.* **2019**, *19*, 12051−12066.
(26) Xu, W.; Zhang, L.; Liu, X. A database of atmospheric nitrogen concentration and deposition from the nationwide monitoring network in China. *Sci. Data* **2019**, *6*, No. 51.
(27) Van Damme, M.; Clarisse, L.; Heald, C. L.; Hurtmans, D.; Ngadi, Y.; Clerbaux, C.; Dolman, A. J.; Erisman, J. W.; Coheur, P. F. Global distributions, time series and error characterization of atmospheric ammonia (NH_3) from IASI satellite observations. *Atmos. Chem. Phys.* **2014**, *14*, 2905−2922.
(28) Clarisse, L.; Clerbaux, C.; Dentener, F.; Hurtmans, D.; Coheur, P.-F. Global ammonia distribution derived from infrared satellite observations. *Nat. Geosci.* **2009**, *2*, 479−483.
(29) Whitburn, S.; Van Damme, M.; Clarisse, L.; Bauduin, S.; Heald, C. L.; Hadji-Lazaro, J.; Hurtmans, D.; Zondlo, M. A.; Clerbaux, C.; Coheur, P. F. A flexible and robust neural network IASI-NH_3 retrieval algorithm. *J. Geophys. Res.:Atmos.* **2016**, *121*, 6581−6599.
(30) August, T.; Klaes, D.; Schlüssel, P.; Hultberg, T.; Crapeau, M.; Arriaga, A.; O'Carroll, A.; Coppens, D.; Munro, R.; Calbet, X. IASI on Metop-A: Operational Level 2 retrievals after five years in orbit. *J. Quant. Spectrosc. Radiat. Transfer* **2012**, *113*, 1340−1371.
(31) Van Damme, M.; Clarisse, L.; Franco, B.; Sutton, M. A.; Erisman, J. W.; Wichink Kruit, R.; van Zanten, M.; Whitburn, S.; Hadji-Lazaro, J.; Hurtmans, D.; Clerbaux, C.; Coheur, P.-F. Global, regional and national trends of atmospheric ammonia derived from a decadal (2008−2018) satellite record. *Environ. Res. Lett* **2021**, *16*, No. 055017.
(32) Wen, Z.; Xu, W.; Li, Q.; Han, M.; Tang, A.; Zhang, Y.; Luo, X.; Shen, J.; Wang, W.; Li, K.; Pan, Y.; Zhang, L.; Li, W.; Collett, J. L., Jr.; Zhong, B.; Wang, X.; Goulding, K.; Zhang, F.; Liu, X. Changes of nitrogen deposition in China from 1980 to 2018. *Environ. Int.* **2020**, *144*, No. 106022.
(33) Xu, W.; Luo, X. S.; Pan, Y. P.; Zhang, L.; Tang, A. H.; Shen, J. L.; Zhang, Y.; Li, K. H.; Wu, Q. H.; Yang, D. W.; Zhang, Y. Y.; Xue, J.; Li, W. Q.; Li, Q. Q.; Tang, L.; Lu, S. H.; Liang, T.; Tong, Y. A.; Liu, P.; Zhang, Q.; Xiong, Z. Q.; Shi, X. J.; Wu, L. H.; Shi, W. Q.; Tian, K.; Zhong, X. H.; Shi, K.; Tang, Q. Y.; Zhang, L. J.; Huang, J. L.; He, C. E.; Kuang, F. H.; Zhu, B.; Liu, H.; Jin, X.; Xin, Y. J.; Shi, X. K.; Du, E. Z.; Dore, A. J.; Tang, S.; Collett, J. L., Jr.; Goulding, K.; Sun, Y. X.; Ren, J.; Zhang, F. S.; Liu, X. J. Quantifying atmospheric nitrogen deposition through a nationwide monitoring network across China. *Atmos. Chem. Phys.* **2015**, *15*, 12345−12360.
(34) Koo, B.; Wilson, G. M.; Morris, R. E.; Dunker, A. M.; Yarwood, G. Comparison of source apportionment and sensitivity analysis in a particulate matter air quality model. *Environ. Sci. Technol.* **2009**, *43*, 6669−6675.
(35) Shearer, S. M.; Harley, R. A.; Jin, L.; Brown, N. J. Comparison of SAPRC99 and SAPRC07 mechanisms in photochemical modeling for central California. *Atmos. Environ.* **2012**, *46*, 205−216.
(36) Wesely, M. L. Parameterization of surface resistances to gaseous dry deposition in regional-scale numerical models. *Atmos. Environ.* **1989**, *23*, 1293−1304.
(37) Seinfeld, J. H.; Pandis, S. N. *Atmospheric Chemistry and Physics: from Air Pollution to Climate change*; WILEY, 1998; Vol. *829*.
(38) Weather Research & Forecasting Model. https://www.mmm.ucar.edu/models/wrf, accessed July 10, 2022.
(39) Ji, H. B.; Shao, M.; Wang, Q. G. Contribution of Meteorological Conditions to Inter-annual Variations in Air Quality during the Past Decade in Eastern China. *Aerosol Air Qual. Res.* **2020**, *20*, 2249−2259.
(40) Wen, W.; Ma, X.; Tang, Y. X.; Wei, P.; Wang, J. K.; Guo, C. W. The impacts of meteorology on source contributions of air pollution in winter in Beijing, 2015−2017 changes. *Atmos. Pollut. Res.* **2020**, *11*, 1953−1962.

(41) Multi-resolution Emission Inventory model for Climate and air pollution research. http://www.meicmodel.org, accessed July 12, 2023.
(42) Kurokawa, J.; Ohara, T.; Morikawa, T.; Hanayama, S.; Janssens-Maenhout, G.; Fukui, T.; Kawashima, K.; Akimoto, H. Emissions of air pollutants and greenhouse gases over Asian regions during 2000−2008: Regional Emission inventory in ASia (REAS) version 2. *Atmos. Chem. Phys.* **2013**, *13*, 11019−11058.
(43) Woo, J. H.; Choi, K. C.; Kim, H. K.; Baek, B. H.; Jang, M.; Eum, J. H.; Song, C. H.; Ma, Y. I.; Sunwoo, Y.; Chang, L. S.; Yoo, S. H. Development of an anthropogenic emissions processing system for Asia using SMOKE. *Atmos. Environ.* **2012**, *58*, 5−13.
(44) Koo, B.; Dunker, A. M.; Yarwood, G. Implementing the decoupled direct method for sensitivity analysis in a particulate matter air quality model. *Environ. Sci. Technol.* **2007**, *41*, 2847−2854.
(45) Li, C.; Martin, R. V.; Shephard, M. W.; Cady-Pereira, K.; Cooper, M. J.; Kaiser, J.; Lee, C. J.; Zhang, L.; Henze, D. K. Assessing the Iterative Finite Difference Mass Balance and 4D-Var Methods to Derive Ammonia Emissions Over North America Using Synthetic Observations. *J. Geophys. Res.:Atmos.* **2019**, *124*, 4222−4236.
(46) Napelenok, S. L.; Pinder, R. W.; Gilliland, A. B.; Martin, R. V. A method for evaluating spatially-resolved NOx emissions using Kalman filter inversion, direct sensitivities, and space-based NO2 observations. *Atmos. Chem. Phys.* **2008**, *8*, 5603.
(47) Brasseur, G. P.; Jacob, D. J. *Modeling of Atmospheric Chemistry*; Cambridge University Press, 2017; Vol. *487*.
(48) Michalak, A. M.; Bruhwiler, L.; Tans, P. P. A geostatistical approach to surface flux estimation of atmospheric trace gases. *J. Geophys. Res. Atmos.* **2004**, *109*, No. 19.
(49) Warner, J. X.; Dickerson, R. R.; Wei, Z.; Strow, L. L.; Wang, Y.; Liang, Q. Increased atmospheric ammonia over the world's major agricultural areas detected from space. *Geophys. Res. Lett.* **2017**, *44*, 2875−2884.
(50) Bai, Z.; Fan, X.; Jin, X.; Zhao, Z.; Wu, Y.; Oenema, O.; Velthof, G.; Hu, C.; Ma, L. Relocate 10 billion livestock to reduce harmful nitrogen pollution exposure for 90% of China's population. *Nat. Food* **2022**, *3*, 152−160.
(51) Zhu, Z.; Zhang, X.; Dong, H.; Wang, S.; Reis, S.; Li, Y.; Gu, B. Integrated livestock sector nitrogen pollution abatement measures could generate net benefits for human and ecosystem health in China. *Nat. Food* **2022**, *3*, 161−168.
(52) Kang, Y.; Liu, M.; Song, Y.; Huang, X.; Yao, H.; Cai, X.; Zhang, H.; Kang, L.; Liu, X.; Yan, X.; He, H.; Zhang, Q.; Shao, M.; Zhu, T. High-resolution ammonia emissions inventories in China from 1980 to 2012. *Atmos. Chem. Phys.* **2016**, *16*, 2043−2058.
(53) Zhang, Y.; Dore, A. J.; Ma, L.; Liu, X. J.; Ma, W. Q.; Cape, J. N.; Zhang, F. S. Agricultural ammonia emissions inventory and spatial distribution in the North China Plain. *Environ. Pollut.* **2010**, *158*, 490−501.
(54) Fu, H.; Luo, Z.; Hu, S. A temporal-spatial analysis and future trends of ammonia emissions in China. *Sci. Total Environ.* **2020**, *731*, No. 138897.
(55) Wang, C.; Cheng, K.; Ren, C.; Liu, H.; Sun, J.; Reis, S.; Yin, S.; Xu, J.; Gu, B. An empirical model to estimate ammonia emission from cropland fertilization in China. *Environ. Pollut.* **2021**, *288*, No. 117982.
(56) Luo, Y.; Zhang, Z.; Li, Z.; Chen, Y.; Zhang, L.; Cao, J.; Tao, F. Identifying the spatiotemporal changes of annual harvesting areas for three staple crops in China by integrating multi-data sources. *Environ. Res. Lett.* **2020**, *15*, No. 074003.
(57) Zhou, F.; Ciais, P.; Hayashi, K.; Galloway, J.; Kim, D. G.; Yang, C.; Li, S.; Liu, B.; Shang, Z.; Gao, S.; Re-estimating, N. H. $_3$ emissions from chinese cropland by a new nonlinear model. *Environ. Sci. Technol.* **2016**, *50*, 564−572.
(58) Chang, Y.; Zou, Z.; Zhang, Y.; Deng, C.; Hu, J.; Shi, Z.; Dore, A. J.; Collett, J. L., Jr. Assessing contributions of agricultural and nonagricultural emissions to atmospheric ammonia in a chinese megacity. *Environ. Sci. Technol.* **2019**, *53*, 1822−1833.
(59) Pinder, R. W.; Adams, P. J.; Pandis, S. N.; Gilliland, A. B. Temporally resolved ammonia emission inventories: Current estimates, evaluation tools, and measurement needs. *J. Geophys. Res. Atmos.* **2006**, *111*, 14.
(60) Balasubramanian, S.; McFarland, D. M.; Koloutsou-Vakakis, S.; Fu, K.; Menon, R.; Lehmann, C.; Rood, M. J. Effect of grid resolution and spatial representation of NH_3 emissions from fertilizer application on predictions of NH_3 and $PM_{2.5}$ concentrations in the United States Corn Belt. *Environ. Res. Commun.* **2020**, *2*, No. 21.
(61) Kong, L.; Tang, X.; Zhu, J.; Wang, Z.; Pan, Y.; Wu, H.; Wu, L.; Wu, Q.; He, Y.; Tian, S.; Xie, Y.; Liu, Z.; Sui, W.; Han, L.; Carmichael, G. Improved inversion of monthly ammonia emissions in China based on the chinese ammonia monitoring network and Ensemble Kalman Filter. *Environ. Sci. Technol.* **2019**, *53*, 12529−12538.
(62) Baker, K.; Scheff, P. Photochemical model performance for $PM_{2.5}$ sulfate, nitrate, ammonium, and precursor species SO_2, HNO_3, and NH_3 at background monitor locations in the central and eastern United States. *Atmos. Environ.* **2007**, *41*, 6185−6195.
(63) Wichink Kruit, R. J.; Schaap, M.; Sauter, F. J.; van Zanten, M. C.; van Pul, W. A. J. Modeling the distribution of ammonia across Europe including bi-directional surface-atmosphere exchange. *Biogeosciences* **2012**, *9*, 5261−5277.
(64) Nesser, H.; Jacob, D. J.; Maasakkers, J. D.; Scarpelli, T. R.; Sulprizio, M. P.; Zhang, Y. Z.; Rycroft, C. H. Reduced-cost construction of Jacobian matrices for high-resolution inversions of satellite observations of atmospheric composition. *Atmos. Meas. Tech.* **2021**, *14*, 5521−5534.
(65) Clarisse, L.; Van Damme, M.; Hurtmans, D.; Franco, B.; Clerbaux, C.; Coheur, P. F. The diel cycle of NH_3 observed from the FY-4A Geostationary Interferometric Infrared Sounder (GIIRS). *Geophys. Res. Lett.* **2021**, *48*, No. 11.

https://doi.org/10.1021/acs.est.4c10878
Environ. Sci. Technol. 2025, 59, 9991−10000